atmosphere

Article

The Ionospheric Responses from Satellite Observations within Middle Latitudes to the Strong Magnetic Storm on 25–26 August 2018

Xuemin Zhang *, Lei Dong and Lei Nie

Institute of Earthquake Forecasting, China Earthquake Administration, Beijing 100036, China
* Correspondence: zxm@ief.ac.cn

Abstract: The multi observations from the China Seismo-Electromagnetic Satellite (CSES) were presented and analyzed during the biggest magnetic storm on 25–26 August in the quiet solar activity year of 2018, together with the Swarm satellite and GNSS TEC (Global Navigation Satellite System, Total Electron Content). The whole tempo-spatial evolutional process was demonstrated in electromagnetic fields and in-situ plasma parameters within the whole magnetic storm time period of three phases, the main phase with quick decrease in SYM-H, the quick recovery phase, and the slow recovery phase. Strong correlations were revealed in time and space between electric fields and electron density. During the main phase, the penetrated electric field was the major factor to induce the injection of electric fields to low latitudes even to the equator and contribute to constructing the double peaks of Ne at altitudes above 500 km of CSES in daytime. In the quick recovery phase, Ne depletion was found in low middle and low latitudes in the daytime, associated with a quick decrease in solar wind dynamic pressure, but in the nightside Ne maintained or increased. Due to the high solar wind speed following the quick recovery phase, it controlled the enhancements in an electric field below 1125 Hz at medium and low latitudes in daytime and produced similar structures in a 225 Hz electric field with the mid-latitude trough of Ne in local nighttime and maintained their equator-ward movements in this time period. Ne/TEC showed typical local time-dependence in this magnetic storm, which illustrated that although the electron density in the ionosphere was mainly caused by this solar activity event, local background environments must also not be ignored for their final evolutional modes.

Keywords: magnetic storm; CSES; Swarm satellites; electric field; electron density

check for updates

Citation: Zhang, X.; Dong, L.; Nie, L. The Ionospheric Responses from Satellite Observations within Middle Latitudes to the Strong Magnetic Storm on 25–26 August 2018. *Atmosphere* **2022**, *13*, 1271. https://doi.org/10.3390/atmos13081271

Academic Editor: Christine Amory-Mazaudier

Received: 5 July 2022
Accepted: 9 August 2022
Published: 11 August 2022

1. Introduction

As the major space weather event, strong magnetic storms have been paid more and more attention due to their severe influences on navigation, communication, space exploration, etc. Studying the storm's impact on the ionosphere can help us to understand the coupling processes and mechanisms among different Earth spheres because the ionosphere is the main media to connect the magnetosphere, atmosphere, biosphere, and lithosphere. Scientists have studied the storm-induced ionospheric disturbances to get their temporal and spatial distribution features at different regions, by using the ground-based detecting technologies, such as ionosonde, GPS TEC, and incoherent scatter radar [1–4]. With the fast development of space exploration technology in last few decades, a lot of new results on magnetic storms have been published on the basis of measurements from satellites, such as COSMOS, DE-1, Cluster, DEMETER, DMSP, COSMIC, Swarm, ICON, GOLD, etc., [5–15], in which some were only on a single case study and some for statistical research. It is illustrated that the combined multi observations provide better opportunities for obtaining the complete evolutional process among Earth's different spheres during the magnetic storms [12].

The penetration electric field is one of the key factors during the interaction process of magnetic storms on magnetosphere and ionosphere, especially on the equatorial ionosphere where it may cause the vertical and horizontal movements of plasma and strengthen the formation of equatorial ionospheric anomalies at higher altitudes. Based on multi instruments on ground and satellites, Cherniak et al. [12] revealed the dusk equatorial plasma bubbles, due to the penetration electric field, during the severe geomagnetic storm on 22–23 June 2015, at the altitudes from ~350 km to ~850 km in the topside ionosphere. By using the dayside multi parameters from satellites of CHAMP, ROCSAT, and DMSP, Balan et al. [16] found the rapid upward drift of plasma in the topside ionosphere at the main phase of positive storms due to the eastward prompt penetrating electric field. Tulasi Ram et al. [17] reported the first observational evidence for simultaneous westward and eastward zonal electric fields at equatorial E and F altitudes in local daytime during 14–15 November 2006, which caused the westward electrojet in the E region, and reinforced the equatorial anomaly in the F region, even to the topside ionosphere at DEMETER satellite altitude of 660 km. Kelly et al. [18] presented a quantitative simulation to explain the storm-enhanced plasma density in the ionospheric tails. Vlasov et al. [19] gave a model simulation about the storm on 15 July 2000, and they found that only penetration of a strong electric field at middle and low latitudes can explain the TEC enhancement in the evening. Due to the complicated characteristics in the coupling mechanism from the magnetic storm on the ionosphere and magnetosphere, many questions still remain in this research domain, besides the urgent requirements for theoretical models.

On 25–26 August 2018, a quiet solar activity year, a strong magnetic storm occurred, which aroused the interests of scientists. Blagoveshchensky and Sergeeva [20] studied ionospheric responses in the European sector by using the parameters of foF2 and GNSS TEC, combing with satellite electron density, to illustrate the ionospheric dynamics. Mansilla and Zossi used foF2, hmF2, and TEC to investigate the characteristics in the South American sector, and they illustrated that thermosphere neutral composition was the main cause for the positive effects during the recovery phase [21]. Bolaji et al. verified the double-humped increase at a middle latitude in the American sector and fountain effects in the low latitudes in the Asian–Australian sector and American sector from observations of GNSS TEC [22]. Combining the observations ground-based geomagnetic field and satellite magnetic field and electron density from CSES, Piersanti et al. identified the principal magnetospheric current system during the different phases of the geomagnetic storm [23]. Astafyeva et al. studied the ionospheric disturbances and irregularities during this geomagnetic storm on the basis of ground-based GNSS, SuperDARN, ionosondes, and satellites, including Swarm, CSES, and DMSP, and they demonstrated the positive ionospheric response in the Asian region driven by $E \times B$ drift during the main phase and small scale irregularities in the American region at mid and high latitudes [24]. By using GNSS ROTI and satellites of Swarm and DMSP, Cherniak and Zakhrenkova found the development of equatorial ionospheric irregularities extending to 25° magnetic latitude and northwest transportation of plasma depletions across midlatitudes [25]. In this paper, the multi measurements were collected from scientific payloads onboard Chinese CSES satellite and the ionospheric disturbances and their interactions were analyzed around the biggest magnetic storm on 25–26 August in the first operating year of CSES of 2018. Combined with other observations, the whole spatio-temporal evolutional processes were investigated, and the ionospheric response characteristics to this event were demonstrated.

2. Background Information

CSES was launched successfully on 2 February 2018, with a circular Sun-synchronous orbit, at an altitude of about 507 km, inclination of about 97.4°, descending node at LT14:00 in daytime and ascending node at LT02:00 in the nighttime, a strictly revisited time period of 5 days, and the observing scale within a latitude of ±65° [26]. Its scientific objectives are to detect the electromagnetic environment and earthquake-related perturbations in the topside ionosphere [27]. There are eight scientific payloads installed onboard, including high precision magnetometer (HPM) to detect the scalar and vector of geomagnetic field in DC-15 Hz [28,29]; search coil magnetometer (SCM) to observe the induced magnetic field within 10–20 kHz [30,31]; electric field detector (EFD) to obtain the three-component electric field in the DC-3.5 MHz frequency band [32]; Langmuir probe (LAP) for electron density (Ne) and temperature (Te) [33]; plasma analyzer package (PAP) for ion-related parameters, such as ion density, temperature, drift velocity, and so on; high energetic particle package (HEPP) to get particle flux and pitch angle for 0.3–3 MeV electrons and 2–20 MeV protons [34,35]; and high energetic particle detector (HEPD) produced in Italy for 2–50 MeV electrons and 15–200 MeV protons [36]; GNSS Occultation Receiver (GOR) and tri-band beacon (TBB) to inverse total electron content (TEC) and Ne profiles [37–39].

To detect the weak ionospheric perturbations induced by earthquakes or other disasters on ground, CSES is designed to operate during low solar activity years with less disturbances from outer space. In the 23rd solar cycle, 2008 was under the extremely low solar activity with the lowest electron density during the DEMETER satellite operation time in 2004–2010 [40], when Ne exhibited different temporal and spatial features with that in high solar activity years [41,42]. Ten years after, 2018 began into another quiet solar year, when CSES may show similar electromagnetic features in the topside ionosphere. The obvious differences between two satellites are, (1) the altitude, for DEMETER at about 710–660 km, and CSES at a lower one about 507 km, much closer to the peak F2 layer in ionosphere; (2) the local time, for DEMETER being LT10:30, with CSES at LT14:00, which is always the occurrence time for maximum electron density each day. Unfortunately DEMETER has ended its operation in 2010, so we do not have chance to compare both similar observations about a same event. However, Swarm satellite is still in-orbit since its launch in November 2013, with the observations of geomagnetic field, Ne, Te, etc., [43]. Swarm consists of three satellites, A, B, and C, in which B was at a higher altitude of 550 km in the beginning and now descends to about 510 km similar with CSES, while paralleled A and C decrease from 450 km to 440 km. Unlike DEMETER and CSES, Swarm does not have a stable local time and it is designed to cover the entire 24 local time for the construction of global geomagnetic field model. These differences among satellites can provide more information for understanding the ionospheric background and its responses to kinds of space events at different times and altitudes.

With the unprecedented spatial and temporal coverage of the global navigation satellite system (GNSS) and the widely distributed ground receivers, the total electron content (TEC) data have been extensively used in ionospheric studies. On the basis of TEC data from hundreds of GNSS stations worldwide, global ionosphere mapping (GIM) was developed to produce the global ionospheric TEC by different institutions, and CODE (Center for Orbit Determination in Europe, Astronomical Institute, University of Bern, Switzerland) is one of them. The GIM TEC, published by CODE, is modeled in a solar-geomagnetic reference frame using a spherical harmonic expansion up to a degree of order 15. Its time interval is 1 h, and the spatial resolution is $2.5^{\circ} \times 5^{\circ}$ in the geographic latitude and longitude. The detailed information on the CODE GIM TEC can be found on the web (http://ftp.aiub.unibe.ch/CODE/IAR_README.TXT (accessed on 21 September 2021), and references included in the document), as well as in the work of Schaer [44].

After half a year following the CSES launch, on 25–26 August 2018, there occurred a strong geomagnetic storm, with the geomagnetic indices varying abruptly (Figure 1). It shows that since UT18:00 on 25 August, the geomagnetic storm started with SYM-H index decreasing quickly, and at 07:00 on 26 August it was detected to the minimum value of -200 nT. At UT13:30, it recovered above -100 nT, and then continued to increase to be above -30 nT on 30 August (Figure 1). So the main phase of this storm took place on 25–26 August within a few hours, and the recovery phase maintained a few days till 30 August. The speed of solar wind began to increase after the quick recovery phase on 26 August and maintained higher values until 29 August. The interplanetary magnetic field and electric field, including the flow pressure exhibited clear variations at the initial phase on 25 August, with Ez increasing firstly and then decreasing quickly, while By and

E decreased with small amplitude firstly and increased largely to the main phase. At the quick recovery phase on 26 August, these four parameters showed strong modulations, at least three times from positive to negative in Bz, By, and E during the second half day of 26 August. The SYM-H (the fifth panel in Figure 1) also presented the minimum value of −200 nT on 26 August, still being −50 nT on 27 August, and up until 29 August, it became bigger than −30 nT, and also ASY-H (the bottom panel in Figure 1) descended to lower than 30 nT on 29 August. This strong geomagnetic storm provides a good opportunity to study the ionospheric response process at middle and lower latitudes on the basis of satellite observations.

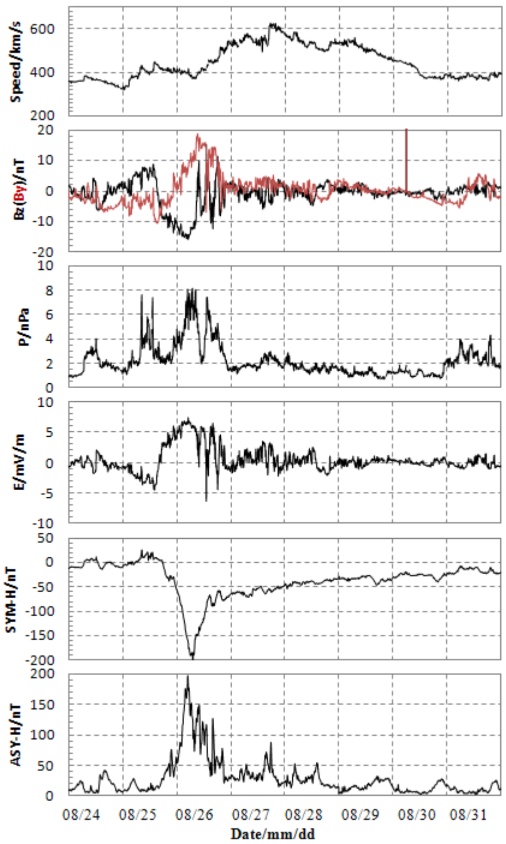

Figure 1. The geomagnetic indices curves from 24 to 31 August in 2018 (from top to bottom are respectively flow speed, interplanetary magnetic field (IMF) Bz (black line) and By (red line), flow pressure, interplanetary electric field (IEF) Ey, SYM-H index, and ASY-H index; all these parameters are published at the website of https://omniweb.gsfc.nasa.gov/form/omni_min.html, accessed on 8 August 2022).

3. Data Analysis

3.1. The Electromagnetic Disturbances on CSES Satellite

In order to detect the three components in electric field, four sensors (a–d) are installed at different directions outside the CSES platform with boom lengths of 5 m, where the detailed position of four sensors (a–d) in the satellite coordinate can be found in the paper of [32]. The waveform data are recorded totally in ULF (ultra low frequency) and ELF (extremely low frequency) bands, but only in burst mode in VLF (very low frequency) band. The spectrum has been calculated and averaged onboard CSES in VLF and HF (high frequency) bands under the survey mode, so the electric field spectra between each two sensors, such as Eab, Ecd, and Ead, have been stored and downloaded directly to the ground [32], where the spectra in VLF and HF bands cannot be transferred to satellite or geographical coordinates again on ground. Figure 2 exhibited the power density values in Ead at six frequency bands selected randomly from VLF spectra from 25 to 29 August 2018, including 225 Hz±, 725 Hz±, 1125 Hz±, 5000 Hz±, 7500 Hz± and 13,500 Hz ± 100 Hz. It can be seen that since the last few hours of 25 August, the electric field signals were enhanced significantly at all chosen frequency points and reached the maximum on 26 and 27 August. On 28 and 29 August, they became weakened but still continued. In the top three panels of Figure 2, the strong disturbed signals not only distributed at high latitudes beyond 50° but also extended to the low latitudinal region at 20–40°, including to the equatorial region of ±20° on 26 August (Figure 2a–c). Compared to the electric field strength at three frequency points shown in Figure 2a–c, the one at 725 Hz showed the maximal values and larger covering area than that at 225 Hz (Figure 2a), especially on 26 August at the equatorial area. Among the three bottom panels in Figure 2d–f, the electric field had the similar evolutional trend with those at lower frequency points in Figure 2a–c, but their strength reduced at least one order in magnitude. During the main phase of this magnetic storm on 25–26 August, the enhanced electric field signals were mainly located in three regions, mid latitude of 40–60° in the northern and southern hemispheres, respectively, and the equatorial area. In addition, Figure 2 illustrates the further interaction between the electric field and high electron density in the equatorial region in local daytime during this geomagnetic storm, obviously at higher frequency points in VLF band relative to their normal weak background (Figure 2d–f). These disturbances were not the direct electromagnetic waves induced by the geomagnetic storm but from the secondary effect due to the enhancement of Ne in this region

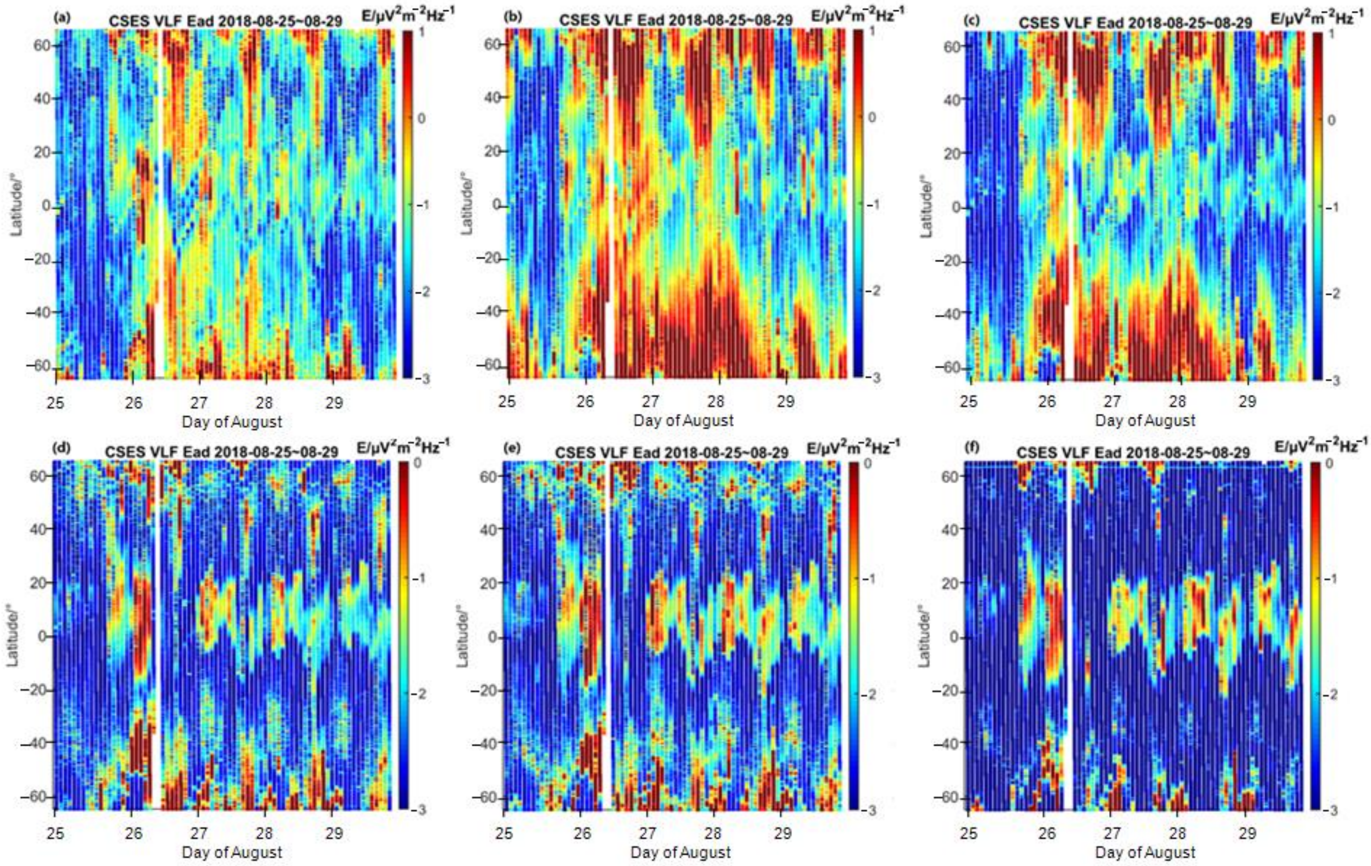

Figure 2. The electric spectrum time series with geographic latitude at 6 frequency bands ((**a**): 225 Hz; (**b**): 725 Hz; (**c**): 1125 Hz; (**d**): 5000 Hz; (**e**): 7500 Hz; (**f**): 13,500 Hz) in local daytime from 25 to 29 August in 2018.

In local nighttime, four frequency points in VLF electric field were selected from CSES and exhibited in Figure 3. The similar variational trend was observed from 25 August until 29 during the whole magnetic storm event. At 225 Hz (Figure 3a), the regular peak structures can be found at latitude of 40–65° each day, typically in the southern hemisphere with strong electric field perturbations. Compared with the background at the quiet time of first half day on 25 August, the enhanced electric field signals can also be distinguished at low latitude (−40)° S–20° N following the final half day of 25 to 27 August, which occurred at different longitudinal region with those at the southern latitude of 40–65° S, but at almost the same time with those at the northern side (Figure 3a). At 725 Hz and 1125 Hz (Figure 3b–c), the regular structures at 40–65° were broken through, while the strong signals propagated to the low latitude of 10–40° at both hemispheres and crossed the equatorial area on 26 and 27 August. At 7500 Hz (Figure 3d), the regular peak electric field structure was maintained at the northern latitude of 40–65°, being similar with those at 225 Hz, but it did not extend to low latitudes, except for the specific peak time on 27 August. From the local nighttime results, the electric field showed significant perturbations on 26 and 27 August, and those signals were even stronger on 27 August, which demonstrates the continuous impact on the ionosphere from this storm during its recovery phase.

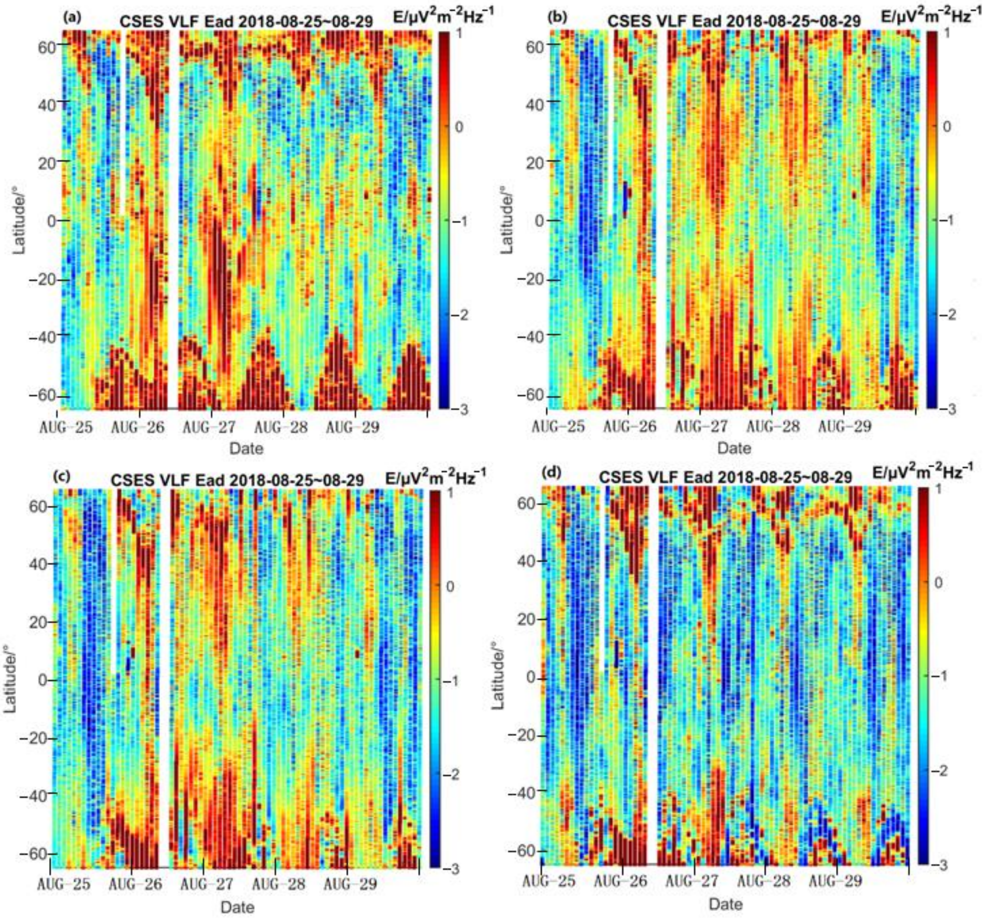

Figure 3. The electric field spectrum values at 6 frequency bands ((**a**): 225 Hz; (**b**): 725 Hz; (**c**): 1125 Hz; (**d**): 7500 Hz) in local nighttime from 25 to 29 August in 2018.

3.2. The Perturbations in Electron Density and Temperature from CSES

In Figures 4 and 5, we plotted Ne and Te from LAP onboard CSES from 25 to 29 August in local daytime and nighttime individually. In dayside of 14 LT, the peak Ne was quite clear at latitudes of 0–20° N. During the main phase of this magnetic storm on 25–26 August, the equatorial peak Ne was further enhanced and spread to −20° S and 40° N (Figure 4a). Then, Ne decreased abruptly to about $10^{10}/m^3$ during the last half of the day on 26 August and increased again from 27 to 29 August, with some larger values above $10^{11}/m^3$ at latitude of (−20)–0° in the southern hemisphere (Figure 4a). As for Te in Figure 4b, it varied reversely with Ne at the equatorial region, with strong decreases of about 1000 K at the main phase of this magnetic storm on 25–26 August and significant increases of above 3000 K in the northern hemisphere, with the decreasing Ne in last half of the day on 26 August. From 27–29 August, the equatorial Te nearing 1000 K was still lower than that of about 1500 K during the quiet first half of the day on 25 August, and the Te valley spread to the southern hemisphere as peak Ne at the equatorial area during all these disturbed days.

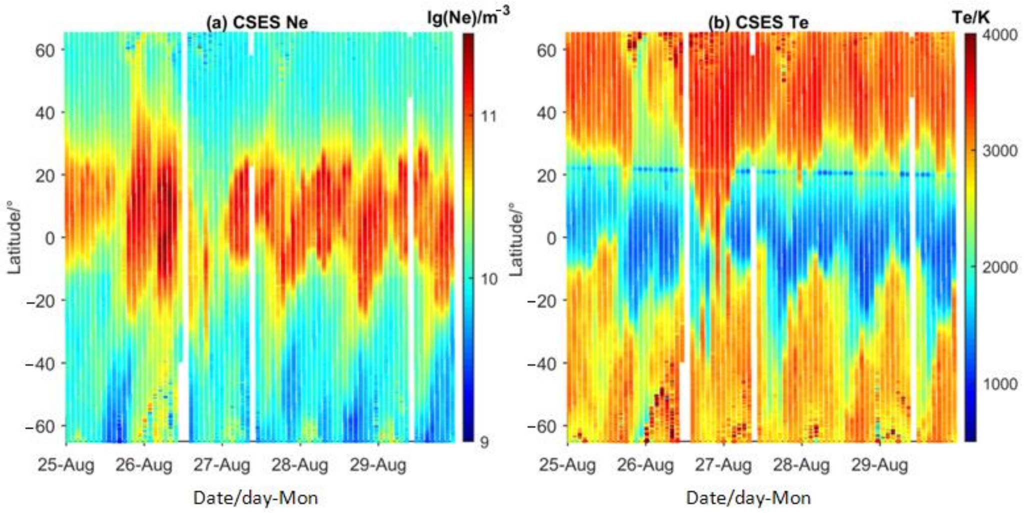

Figure 4. The electron density (**a**) and electron temperature (**b**) in local daytime from 25 to 29 August in 2018.

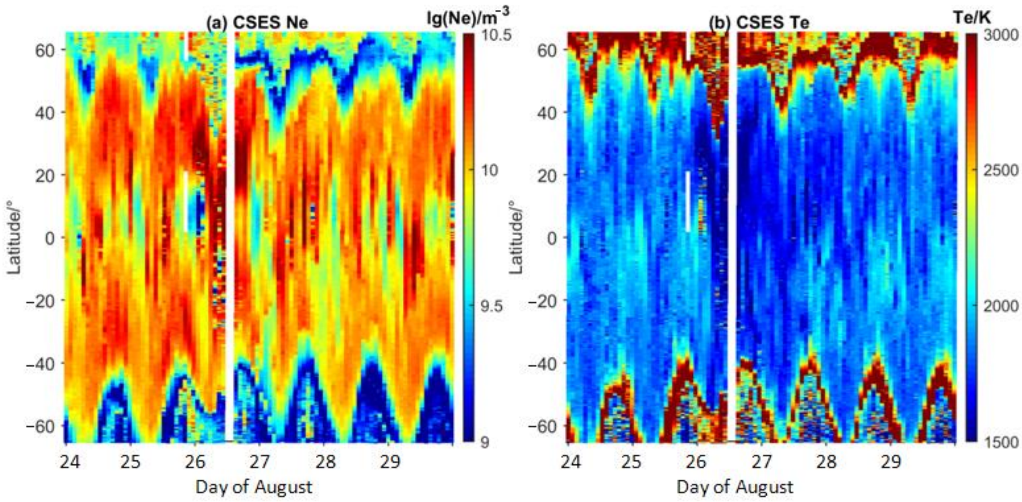

Figure 5. The electron density (**a**) and electron temperature (**b**) in local nighttime from 24 to 29 August in 2018.

In nightside of 02 LT, as shown in Figure 5, peak Ne values were located at 20–40° at both hemispheres, partly at the equatorial area, which is largely different with those in the local daytime in Figure 4. To reveal the background information, one more day on 24 August was included in Figure 5. It can be seen that, during this magnetic storm, Ne was enhanced mainly on 26 August between the latitude of ±40°, with the simultaneous decrease in Te at the same region. Another interesting phenomenon in local nighttime is the regular daily Ne valleys with a clear boundary at mid latitudes of 40–65°, also known as the midlatitude trough, where Ne decreased at least one order of magnitude relative to the Ne around latitudes of 30°, typically in the southern hemisphere during the whole studied time period. To illustrate the changes in the position of the midlatitude trough of Ne, Table 1 listed the latitudes of the first Ne minimum, near to equator-side in the northern and southern hemisphere in UT06-08 and 18–20, where "/" represents that the minimum was still not occurring in the observational scale of CSES, within a latitude of 65°. During this storm, the latitudes of Ne trough in the southern hemisphere moved inside −60° S at the beginning of 26 August when it should be beyond −65° S at the same time period in other days, and the northern latitude was 33.24° N, moving 20° to the south relative to 24 August at 53.54° N and about 15° relative to that on 25 August at about 48.65° N. The obvious trough region in Ne maintained from 27–29 August, and its top equatorward minimum boundary was closer to 41° latitude in the southern hemisphere, being 5–8° to the north compared with those on 24–25 August (Table 1). Compared with the electric field at 225 Hz and 7500 Hz in Figure 3a,d, the Ne trough at latitudes of 50–65° was just corresponding to the strong disturbed region in ELF/VLF electric field, illustrating the significant correlation in both parameters. Te in local nighttime showed an obvious peak structure at a latitude of 40–65°, in contrast with Ne. The regional peak Te was enhanced on 26 August in the northern hemisphere, with its top boundary further extending to the equator, when the Te peak boundary in the southern hemisphere also moved to the equator about 10°. From 27–29 August, the whole Te peak structure at middle latitude maintained the same equatorward movement as those of Ne trough.

Table 1. The first minimum position of midlatitude trough of Ne from CSES during 24 and 29 August.

Day of August	24	25	26	27	28	29
Latitude in northern hemisphere at UT 06–08/° N	53.544	48.65	33.24	42.53	47.11	45.24
Latitude in southern hemisphere at UT 06–09/° S	/	/	55.60	64.11	/	/
Latitude in northern hemisphere at UT 18–20/° N	59.41	57.20	57.46	49.54	58.15	58.45
Latitude in southern hemisphere at UT 18–20/° S	49.80	46.04	40.71	41.60	41.66	42.83

To illustrate the interaction of electric field and Ne during this magnetic storm, the first orbits were selected in the dayside and nightside, two on 26 August to represent the main phase and two on 28 August for recovery phase, respectively. The correlation between electric field spectra at 225, 725, 1125 Hz and Ne was computed at different latitude scales, with the interval of 15° along the same orbit. As seen in Table 2, in the dayside of the main phase on 26 August, the positive correlation values were detected at the equatorial area at a latitude of 0–30° N with r > 0.9 at all three frequency bands, but during the recovery phase on 28 August, high positive correlations were revealed at 45–60° S with r > 0.8, and r = 0.79 at 0–15° S at 225 Hz. As for the nightside, r decreased totally relative to those in the dayside but with high negative values of r < −0.5 occurring at 45–60° N and 45–60° S. Large positive correlations with r>0.6 were shown at 15–30° S at 225 Hz and 30–45° S at 1125 Hz on 26 August, which demonstrates the strong penetration of an electric field during the main phase, with the increasing Ne in middle and low latitudes, especially in the southern hemisphere. Nightside data exhibited the enhanced electric field mainly at middle latitudes of 30–45° S while partially contributing to those at 0–15° S.

Table 2. The correlation r of E/Ne at different latitudes from CSES on 26 and 28 August. The bold values present the maxima.

Latitudes	45–60° S	30–45° S	15–30° S	0–15° S	0–15° N	15–30° N	30–45° N	45–60° N
r of E/Ne in dayside on 26 August with E at 225 Hz	0.040	0.78	−0.42	0.83	**0.91**	**0.93**	−0.24	−0.32
725 Hz	−0.32	0.61	−0.68	0.47	**0.93**	0.85	**−0.95**	−0.34
1125 Hz	−0.51	0.81	−0.71	0.55	**0.94**	**0.90**	**−0.96**	−0.075
r of E/Ne in dayside on 28 August with E at 225 Hz	**0.83**	0.53	0.20	0.79	0.31	−0.33	−0.34	−0.034
725 Hz	−0.27	0.18	0.60	**−0.88**	0.30	−0.58	−0.65	0.36
1125 Hz	−0.54	0.088	−0.31	0.15	0.56	−0.26	−0.70	0.43
r of E/Ne in nightside on 26 August with E at 225 Hz	−0.59	0.17	**0.61**	0.43	−0.044	−0.51	0.057	**−0.65**
725 Hz	−0.35	0.35	0.15	0.072	−0.0089	0.40	0.27	**−0.61**
1125 Hz	−0.48	**0.64**	0.13	0.42	0.049	0.036	0.20	−0.59
r of E/Ne in nightside on 28 August with E at 225 Hz	−0.50	−0.034	0.015	0.52	−0.33	0.064	−0.069	−0.59
725 Hz	−0.53	0.59	0.078	0.40	0.10	−0.24	0.14	−0.53

Table 2. *Cont.*

Latitudes	45–60° S	30–45° S	15–30° S	0–15° S	0–15° N	15–30° N	30–45° N	45–60° N
1125 Hz	−0.51	**0.68**	0.085	0.37	0.076	−0.096	−0.091	**−0.76**

4. Discussion on the Corresponding Processes in Ionosphere

4.1. The Comparison of Plasma Parameters at Different Altitudes

Among the three satellites of Swarm, Ne, and Te from satellite A and B, different altitudes were collected and plotted in Figure 6. For Swarm-A, the local daytime was mainly between 13:00–15:00 at low and middle latitudes from 24–29 August, being close to the local time of CSES at 14:00. However, the altitude of Swarm-A was 435–455 km, about 60 km lower than CSES. As shown in Figure 6, the similar evolutional features were detected from Swarm-A as those on CSES, with significant increases in Ne in the equatorial area following the last few hours on 25 August to the first few hours on 26 August and the enhanced equatorial Te valley at the same time. From 27–29 August, the peak equatorial Ne was still enhanced, and the double peaks were illustrated clearly at the altitude of Swarm-A. In the meantime, the strong valley in Te continued with an obvious extension to the southern side.

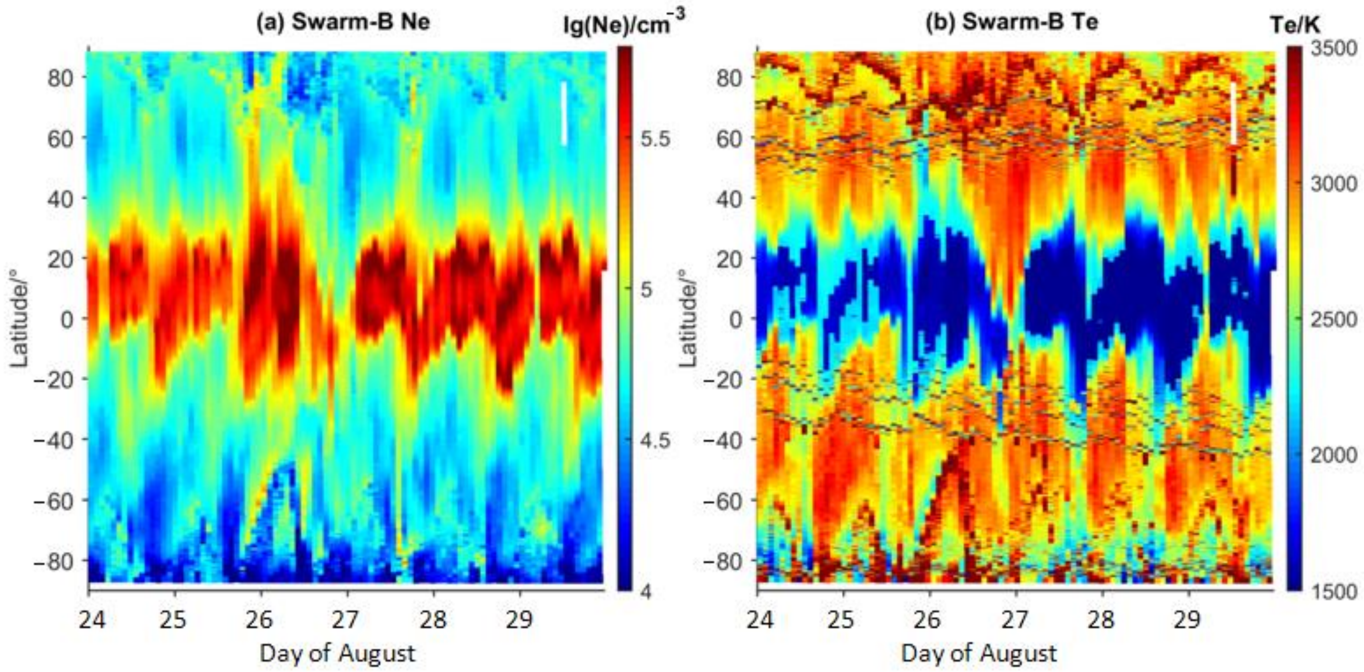

Figure 6. The electron density (**a**) and electron temperature (**b**) from Swarm-A in local daytime during 24 to 29 August in 2018.

For Swarm-B, its altitude was close to CSES, but its local daytime from 24–29 August was mainly in the morning from about 08:00–11:00. In Figure 7 Ne from Swarm-B was relatively smaller than that on Swarm-A, due to its higher altitude and the early local time. Around this magnetic storm, the obvious increase in equatorial Ne can be found in the last few hours on 25 August. However, on 26 August, there was no distinct enhancement most of the time throughout the whole day. Since 27 August, the typical equatorial peak of Ne recovered again. From the temporal distribution of Te in Figure 7, its minimum values at the equatorial area occurred on 27 and 28 August, during the recovery phase, not in the main phase. These phenomena demonstrate that the difference in local time, as Swarm-B will severely influence the distribution features of Ne and Te during the magnetic storm.

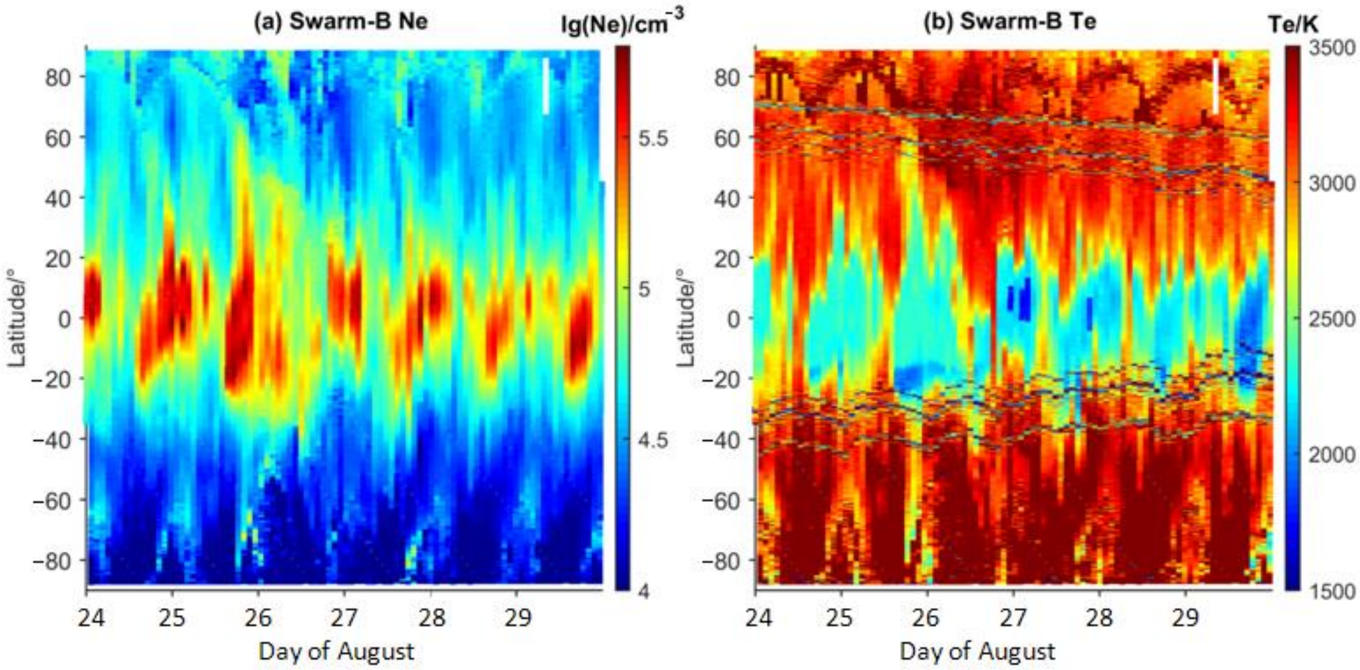

Figure 7. The electron density (**a**) and electron temperature (**b**) from Swarm-B in local daytime during 24 to 29 August in 2018.

In ionospheric research, scientists use the GNSS signals to obtain the total electron content (TEC) for monitoring the ionospheric environment. Here we collected the global TEC mapping data published by CODE [44] and transferred the universal time to local time to compare with the observations of CSES and Swarm. Figure 8 showed the global TEC at local time of 09, 11, 13, and 15 for each day from 25 to 28 August. By the panels at LT09:00 in four days, the increase in TEC was not so clear at the main phase on 26 August, which was consistent with that on Swarm-B. At LT 13–15, the double peaks at the equatorial area were enhanced on 26 August (Figure 9b), especially in the eastern hemisphere. Until 28 August (Figure 9d), the double peaks occurred almost globally, which verified the observations of Ne from Swarm-A at lower altitudes. At the altitude 507 km of CSES, the double peak effect was only distinct on 26 August at the main phase of the storm, but during 27–29 it was widely flat without double peaks.

Compared with the observations of foF2 and TEC in South American sector [21], TEC from CODE exhibited little increase at LT09 on 26 August relative to that on 25 August, and an obvious increase at LT 11–15 from 26–28 August, even with double peaks occurring at low latitudes of this region at LT 13–15 on 28 August during the slow recovery phase, while the small decrease in foF2 at the equator and low latitude at the initial stage of the main phase was not revealed in our results. In the European sector, due to the low values in TEC from CODE at middle latitudes, no obvious increase occurred at latitudes of 45–60° N, as shown in [20], on 26 August, but in the African sector, the equatorial increase was significant at LT09 and 11 on 26 August and at LT13 and 15, even continuing, on 28 August, as shown in Figure 8. Based on the observations from Jason satellites at altitudes of about 1330 km, the evening equatorial ionospheric anomaly (EIA) were illustrated around LT21 at the Pacific region of longitudes 180~150° W during the main phase on 26 August [25]. In comparison with the nighttime Ne at altitude of 507 km from CSES in Figure 5, Ne at low and middle latitudes indeed increased at the main phase on 26 August, but the two peaks at latitudes of 20–40° were not newly constructed, due to this magnetic storm on 26 August relative to those on 24 and 25 August. The enhanced EIA was obviously presented in the dayside from Ne of CSES and Swarm satellites in Figures 6 and 7, and at the Asian sector of longitudes 60–120° E from TEC of CODE in Figure 8 that is consistent with the results about the Asian–Australian sector in [22,24]. The different observations demonstrated the different effects of magnetic fields on ionosphere at different altitudes and different times.

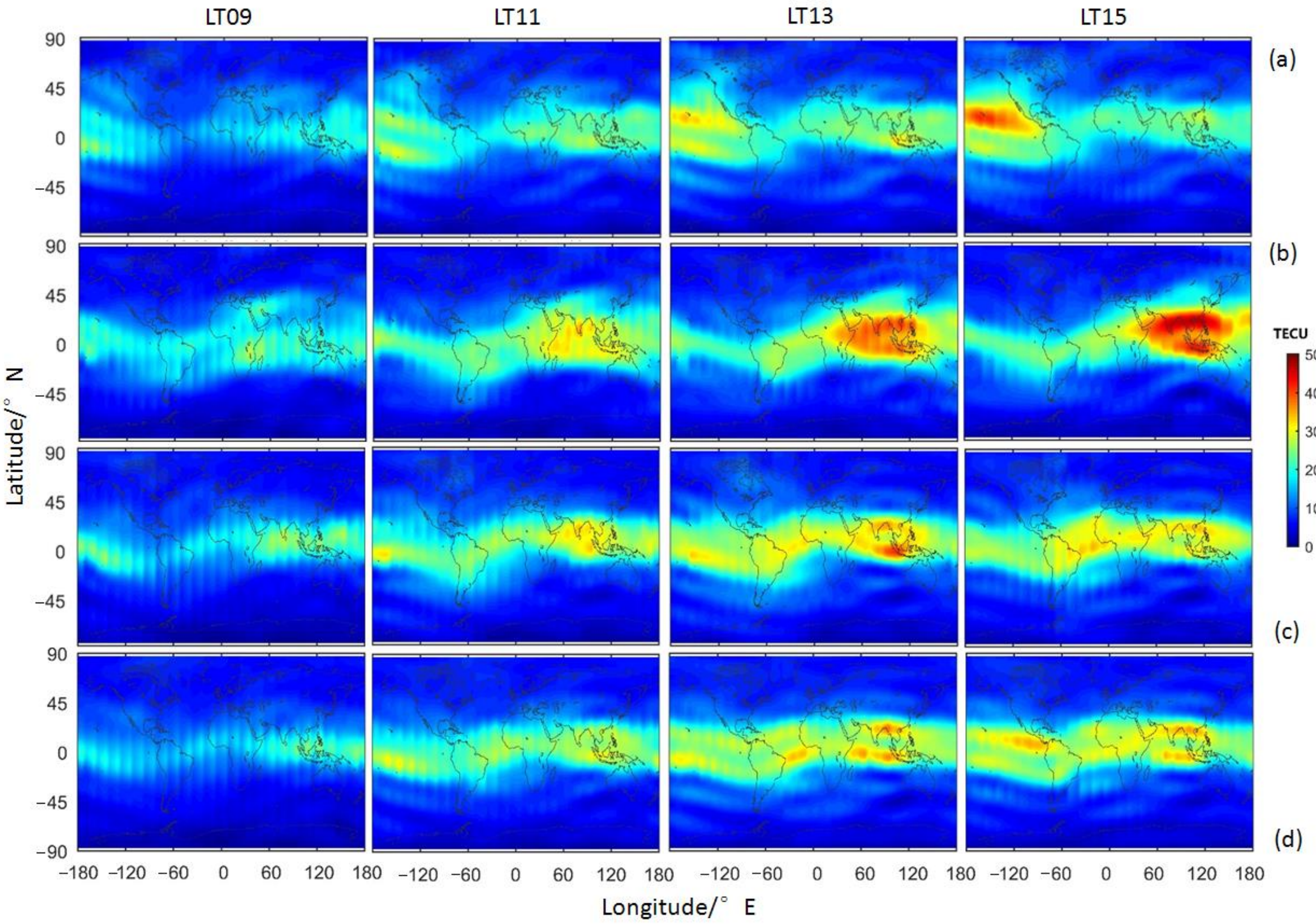

Figure 8. The global TEC mapping at local time 09:00 to 15:00 during 25–28 August in 2018 ((**a**)–(**d**) represents 25–28 August, respectively).

To confirm this feature of local time dependence for electron density to magnetic storms, the 2 h-averaged curves of TEC have been calculated at different latitudes for Swarm A and B in local day and nighttime, respectively. As shown in Figure 9a, around local daytime of 14:00 for Swarm A, the maximum occurred around the beginning of 26 August, corresponding to the minimum of SYM-H, as shown in Figure 1; while the minimum occurred at the end time of 26 August, and then during 27–31, the maxima of each day are larger than that on 24 August at the quiet time. At the local nighttime of 02:00 for Swarm A (Figure 9b), the maximum occurred at the main phase of this magnetic storm, and then there were big differences in different latitudes, where for a latitude of 45–60°, the minimum occurred on 27 August, before all latitude curves slowly recovered to their normal state until Aug. 31. Compared with Swarm B in local daytime around 09:00 (Figure 9c), the big differences occurred during the recovery phase of 27–31, in which the maxima of 27–28 August did not go back to the normal level as it was at the beginning on 25 August; it was even lower from 29–31 August, which is not like the higher TEC in LT14:00 from 29–31 August, as shown in Figure 9a. In LT21:00 (Figure 9d), the lowest maximum was exhibited on 28 August at all low and middle latitudes, but on 29 August, it quickly recovered to the normal values, similar to those in 24–25 August. The daily minima from 24–31 August occurred on 29 August at LT09:00 or 21:00, typically at latitudes of 30–45° and 45–60°. From these TEC curves, it can be found that the electron density has significant local time dependence with four kinds of variational trends corresponding to four different local times either at the main phase or the recovery phase, and the magnetic storm affects all the trends at lower and middle latitudes. The nightside enhancement of TEC on 26 August in Figure 9d is similar to LT21with those from Jason satellites in [25], and the TEC in latitudes of 15–30° even exceeded that of 0–15°, which is totally different with that in Figure 9b at LT02 with almost no changes on 26 August, compared to those from 24–25 August. So the mid latitude enhancement of electron content in topside ionosphere can be further confirmed in the nightside at LT 21 from satellites of SWARM-B and Jason-2, three by our results and [25].

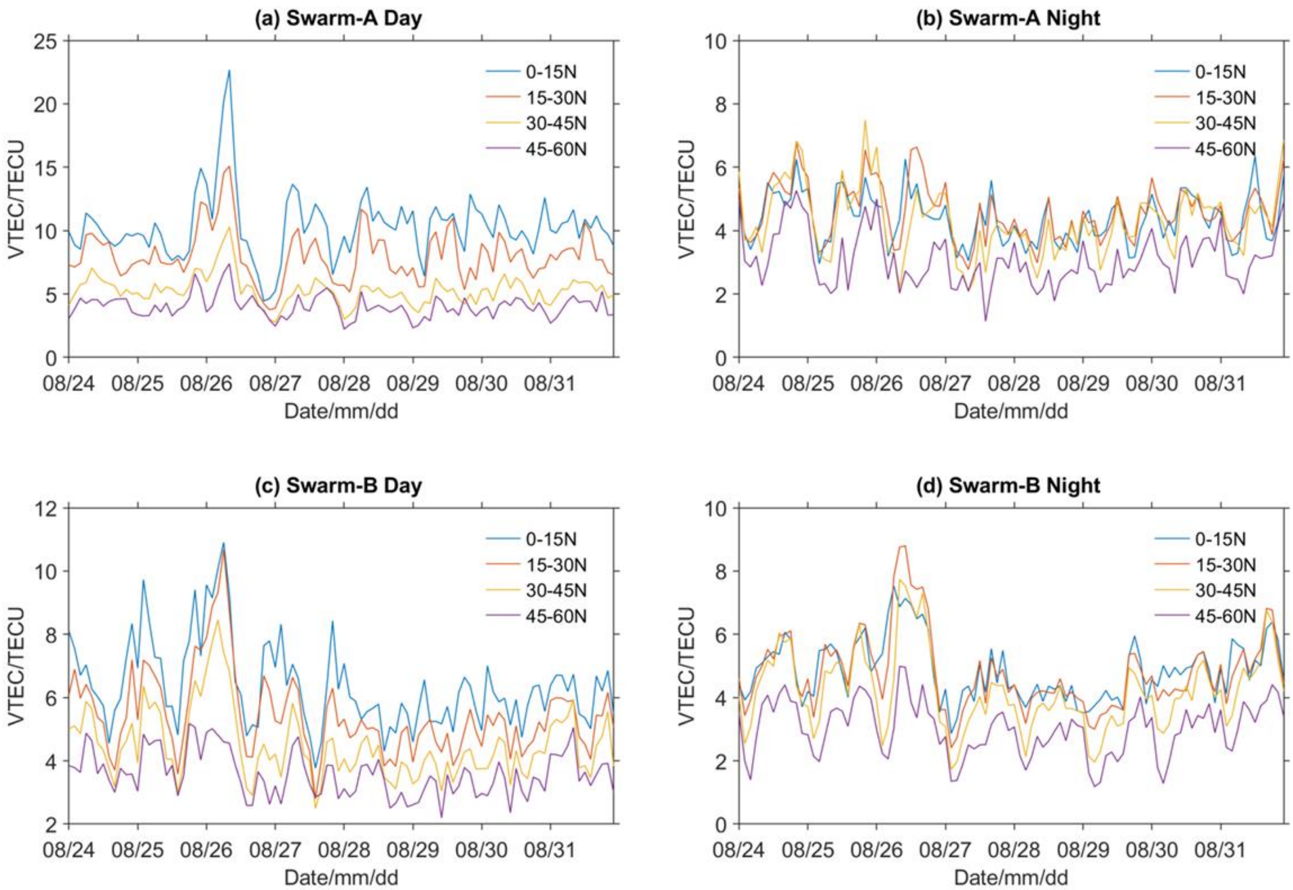

Figure 9. The 2 h-averaged TEC curves at different latitudes onboard Swarm A and B during 24–31 August in 2018 ((**a**,**b**) represents Swarm A and (**c**,**d**) represents Swarm B at local day and nighttime).

The PAP on CSES recorded the ion-related parameters, including ion composition, density, temperature, and drift velocity. However, since the last half of the month in March 2018, the number of ions reduced largely and the hydrogen and helium ions cannot be distinguished, possibly due to the contamination from the unknown materials. So the absolute measurement from PAP is questionable, but the relative measurement may be taken as a reference due to its stable observing condition and results. By comparing the ion drift velocity along the revisited orbits at UT 06:00 of #3117-0 and #2813-0 on 26 August and 6 August, respectively, it is found that at the equatorial area, the ions were accelerated in a northeast direction, but there was almost no change in vertical drift velocity of ions, which illustrates that a vertical electric field was overlapped on the equatorial ionosphere on 26 August relative to the normal state on 6 August, and it caused the horizontal movement of ions due to $E \times B$ effect. Different observations demonstrated that the strong electric field was only excited at the main phase of this magnetic storm and influenced the distribution of Ne at the equatorial area to enhance the double peaks. During the recovery phase, the double peak effect was maintained at the peak region of F2 layer to the altitude of Swarm-A at about 450 km but not to the height of CSES of 507 km.

Ren et al. [45] used the multi observations to study the ionospheric responses during the recovery phase of this storm, and they found that the high speed of solar wind from 27–30 August was effective in changing the aurora and convection patterns, and the high solar wind velocity contribute to enhance the daytime eastward electric fields in the low-latitude ionosphere and thus affect the ionospheric fountain structure at the equatorial region. To verify this feature, the linear correlation (r) was calculated between solar wind speed, pressure, and the TEC as listed in Table 3. Negative correlation was exhibited in speed/TEC either in local daytime or nighttime from SWARM A and B, while mostly positive correlations are found in P/TEC (Pressure/TEC). During the whole magnetic storm event time period of 24–31 August, the absolute correlations of speed/TEC in nightside were larger than those in dayside, which illustrates the enhanced action from solar wind speed on the TEC in the nightside. For the recovery stage during 27–31 August, the negative correlation exceeded -0.5, being larger than that in P/TEC, which demonstrates that solar wind speed may play an important role at low and middle latitudes in the nightside of LT21, especially during the recovery phase of this storm. The pressure contributed a lot during the whole event time of 24–31 August, and the correlation decreased during the recovery phase of 27–31 August and smaller than that in r of speed/TEC. Compared with our results in Figure 2, the electric field at the three extremely low frequency bands under 1125 Hz penetrated into the middle and low latitudes not only in the main phase but also continued until even 29 August during the whole recovery phase, where the high solar wind speed also maintained larger than 400 km/s in this time period. So the penetration of the electric field was confirmed by the observations at ULF and ELF frequency bands of CSES, and the effects on the double peaks of Ne at the equatorial area in the daytime, as shown in Figure 6, could be well explained by the simulation of Ren et al. [45]. Akala et al. [46] discussed the solar origin of this magnetic storm and its response in the ionosphere at medium and low latitudes, and they also illustrated the prompt penetration electric field, contributing to equatorial anomaly crests within $\pm 15°$ of magnetic latitudes. In our research, as shown in Figures 4 and 6, the geographic latitudes of equatorial ionization anomaly crests were located within $\pm 20°$, but the latitudinal differences between two crests were within 20°, although they were pushed southward overall during the recovery time period. As for the local time effects, they pointed out that the PRE-related $E \times B$ drift provide a conducive environment for irregularities generation during post-sunset hours at low latitude regions, especially in the Pacific Ocean west sector, but it is possibly not suitable to explain the variations, as shown in Figure 9b, with no significant enhancement during the main phase and continuous low values in the recovery phase. The variation mode in Figure 9b may not only include the local time effects, but the longitudinal and altitudinal influences cannot be ignored, which is similar to the variations of TEC in the South America sector [46] with no significant enhancement at main phase. Although the penetration electric fields still existed in local nighttime, as observed by CSES in Figure 3, the electron density at different positions (longitude and latitude) and local times and altitudes are still controlled by the local plasma environment of the ionosphere, including the distribution of O/N2, etc., [20,46]. Here, the altitude is also taken into account because the local nighttime for Swarm-A and CSES are close to each other at around 02:00, but CSES showed clear enhancement of Ne at the main phase; although some depletion structure existed at equatorial area, the TEC enhancement was totally covered up from Swarm-A at medium and low latitudes.

4.2. The Movement of Midlatitude Trough during the Magnetic Storm

On the basis of the DEMETER satellite in local nighttime around 22:30 at the altitude of 670 km during 2006–2009, Chen et al. [47] studied the midlatitude trough and the plasmapause in the ionosphere by using Ne, Te, and whistler counts, respectively, and their statistical results illustrated that both of them moved equatorward during the magnetic disturbed conditions, while the midlatitude trough would occur in the equatorward side of the plasmapause when $Kp \geq 6$. Onboard CSES, no whistler data was automatically detected in electric field as DEMETER to determine the position of the plasmapause, so only the midlatitude trough will be discussed here, based on the observations of Ne and Te from LAP. As shown in Figure 5, the nighttime midlatitude trough can be clearly distinguished in both hemispheres at the altitude of the CSES at about 507 km, with a decrease in Ne and an abrupt increase in Te beyond a latitude of 40°. During this magnetic storm on 25 August, the daily northmost point of the midlatitude trough boundary moved about 5° northward in the southern hemisphere, relative to that on 24 August. On 26 August, the daily southmost point of the midlatitude trough reached a latitude of about 30° N in the northern hemisphere, while the southmost boundary in the southern hemisphere drifted to a latitude of −50° S, where it was always beyond −65° S at normal conditions in the first few hours on 24 August and 25. Therefore, the troughs all shifted their position of 15° to the equator at both hemispheres. During the recovery phase in 27–29 August, the northmost latitude of the southern trough maintained at about −40° S, with equatorward movement of about 5° relative to that on 24 August. In the northern hemisphere, the northmost boundary of the trough moved from 65° N to 55° N in 26–27 August, being still at 60° N in 28–29 August. Therefore, during the whole event, the local nighttime midlatitude trough observed from CSES shifted equatorward about 15° at the main phase with the biggest Kp = 7 and maintained a 5° equatorward movement during the recovery phase for more than three days.

Table 3. The correlation between TEC from Swarm satellites and solar wind speed and pressure. The bold values present the maxima.

Satellite LT Latitudes/° N	**Swarm-A 14 LT 0–15 15–30 30–45 45–60**	**Swarm-B 09 LT 0–15 15–30 30–45 45–60**	**Swarm-A 02 LT 0–15 15–30 30–45 45–60**	**Swarm-B 21 LT 0–15 15–30 30–45 45–60**
r of speed/TEC in 24–31 August	−0.10 −0.22 **−0.35** −0.19	−0.26 −0.27 **−0.34** −0.33	−0.37 −0.37 −0.430 **−0.45**	**−0.43** −0.40 −0.40 −0.41
r of P/TEC in 24–31 August	0.35 0.38 **0.54** 0.43	0.37 **0.50** 0.47 0.37	0.098 **0.19** −0.040 −0.13	**0.64** 0.60 0.44 0.32
r of speed/TEC in 27–31 August	−0.013 −0.104 **−0.26** −0.054	0.026 −0.04 **−0.20** −0.16	−0.35 −0.40 **−0.51** −0.42	−0.51 −0.52 **−0.53** −0.46
r of P/TEC in 27–31 August	0.096 0.11 0.16 **0.20**	0.088 0.22 0.28 **0.35**	0.033−0.019 −0.050 **−0.064**	0.32 **0.37** 0.32 0.29

Figure 10 presented the local nighttime Ne and Te on Swarm-A, in which the boundary of the midlatitude trough was quite clear, especially its topmost part at a high latitude of 60–70° N in the northern hemisphere, due to its global coverage. In the southern hemisphere, no high values of Ne occurred again at a high latitude beyond 60°, so this midlatitude trough covered quite a large area, even to −90° S, which is totally different compared to that in the northern hemisphere. Compared with the results from He et al. [48] by using COSMIC observations, the large covering area of the trough in the southern hemisphere should be related to its seasonal variations of lower Ne in winter days. Around this magnetic storm, Swarm-A exhibited the same characteristics with CSES in the midlatitude Ne trough and Te peak, with significant equatorward movement of more than 15° at the main phase and maintained a small shift of about 5° during the recovery phase in the local nighttime.

As for the shift of the midlatitude trough, Deminov et al. [49] introduced an empirical model to qualitatively interpret the dynamics of the position of the trough at 430 km altitude during the main phase, and their results showed step-like equatorward movement in the pre-midnight hours in the main phase of an intensive magnetic storm, while the solar local time and magnetic local time were considered and compared in the new model due to the dependence of the trough on them [50]. The local time of CSES and Swarm-A was beyond midnight at about 02:00, and both of them showed abrupt movement in the northern hemisphere at the main phase on 26 August, but a smooth boundary was revealed at the same time in the southern hemisphere, in which the different season and regional effects should be taken into account. The strong correlations between electric fields and Ne were illustrated by CSES in local nighttime with the similar spatial distribution characteristics of electric fields at 225 Hz and Ne to depict the mid-latitude trough in the northern and southern hemispheres, as in Figures 3 and 5, including with Ne from Swarm-A in Figure 10, which demonstrates the strong interaction of ULF/ELF electric field with electron density at medium latitudes at local nighttime, during the whole magnetic storm time period.

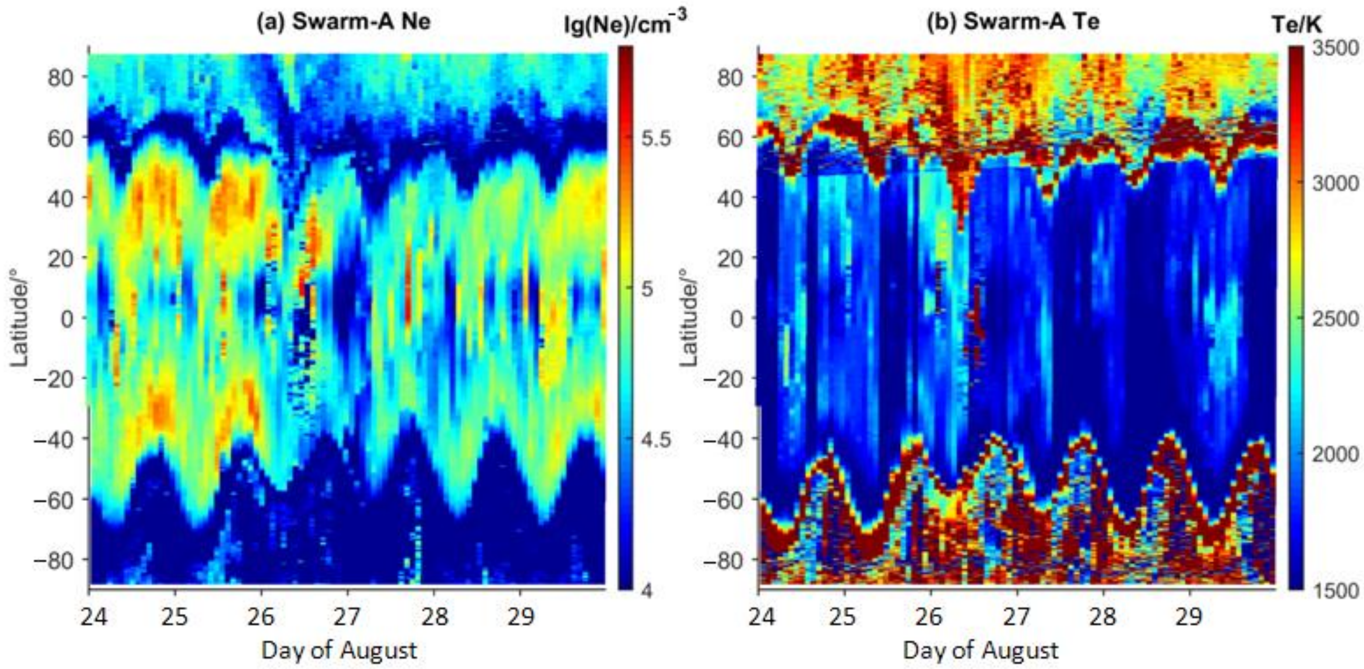

Figure 10. The electron density (**a**) and electron temperature (**b**) from Swarm-A in local nighttime during 24 to 29 August in 2018.

5. Conclusions

This strong magnetic storm from 25–29 August in 2018 can be divided into three phases, the main phase with a fast decrease in SYM-H index from 25–26 August; the quick recovery phase with a quick increase in SYM-H during the last half of the day on 26 August; the slow recovery phase from 27–29 August. Based on the multi observations from CSES and other satellites, some interesting ionospheric characteristics at medium and low latitudes can be concluded as the following, responding to the three magnetic storm phases.

(1) Typical penetration signals of electric field were illustrated during three storm phases from the ultra-low frequency band to very low frequency band in either local daytime or nighttime from CSES. Ne showed strong correlation with electric fields in extremely low frequency bands under 1125 Hz in local daytime at 0–30° N and 15–45° S in the nightside during the main phase, while in the recovery phase, the high positive correlation between electric fields and Ne were concentrated at 0–15° S, 45–60° S in the dayside, and in the nightside 30–45° Swhere the penetration of electric fields and enhanced Ne were concentrated at. The interaction of electric fields with ionospheric electron density decreased in the nightside both at the main phase or recovery phase, compared to in the dayside.

(2) High solar speed generated significant effects during the recovery phase, especially the nighttime ionosphere, with lower Ne in 27–28 August at low latitudes. Higher negative correlation occurred with $r < -0.5$ of speed/TEC in the nightside during the recovery phase, while solar wind pressure contributed less during the recovery phase with $r < 0.4$ than those in main phase with $r > 0.6$.

(3) Multi observations reveal the local time dependence of Ne and TEC to this magnetic storm, with four local time variation modes presented. The depletion of Ne is much

clearer at low latitudes in local daytime at a fast recovery time on 26 August, but it is obvious at medium and low latitudes in local nighttime during the slow recovery time of 27–29 August. The electric field observations from CSES in the dayside of 14LT and the nightside of 02LT demonstrated the strong penetration electric at middle and low latitudes in extremely low frequency and very low frequency both in the main phase and recovery phase, but some regions still exist with a correlation $r < 0.1$, which was also revealed in many small r values of speed and pressure with TEC. The regional ionospheric response needs to consider the local plasma and neutral particle environment, as suggested in other research.

Author Contributions: Data curation, X.Z., L.D. and L.N.; Formal analysis, X.Z.; Investigation, L.D.; Methodology, X.Z. and L.N.; Writing—original draft, X.Z.; Writing—review and editing, X.Z. All authors have read and agreed to the published version of the manuscript.

Funding: This work was funded by the National Natural Science Foundation of China (NSFC) under Grant Agreement No. 41674156 and the National Key R&D Program of China under Grant No. 2018YFC1503506.

Institutional Review Board Statement: This study does not require ethical approval.

Data Availability Statement: CSES data is available at the website https://www.leos.ac.cn (accessed on 21 September 2021), Swarm satellite data is at the website http://earth.esa.int/swarm (accessed on 21 September 2021), GIM TEC from CODE is available at http://ftp.aiub.unibe.ch/CODE/ (accessed on 21 September 2021), and the solar activity and magnetic index are at the website https://omniweb.gsfc.nasa.gov/form/omni_min.html (accessed on 21 September 2021).

Acknowledgments: This paper is supported by NSFC project (41674156), National Key R&D Program of China (Grant no. 2018YFC1503506), and Dragon-5 plan (#59308). The authors thank the CSES satellite center (www.leos.ac.cn (accessed on 21 September 2021)) after registration and Swarm satellite center (http://earth.esa.int/swarm, accessed on 21 September 2021) for providing the data and appreciate ISSI-BJ for supporting our international team (#33) in 2019. The solar wind and magnetic index data are from the website of https://omniweb.gsfc.nasa.gov/form/omni_min.html (accessed on 21 September 2021), and CODE TEC is downloaded from the website of http://ftp.aiub.unibe.ch/CODE/2018/ (accessed on 21 September 2021).

Conflicts of Interest: The authors declare no conflict of interest.

References

1. Grigorenko, E.I.; Lysenko, V.N.; Taran, V.I.; Chernogor, L.F. Results of Radar Studies of Processes in the Ionosphere that Accompanied the Strongest Geomagnetic Storm of September 25, 1998. *Usp. Sovrem. Radioelektron.* **2003**, *9*, 57–94.
2. Grigorenko, E.I.; Lysenko, V.N.; Pazyura, S.A.; Taran, V.I.; Chernogor, L.F. Ionospheric disturbances during the severe magnetic storm of November 7–10, 2004. *Geomagn. Aeron.* **2007**, *47*, 720–738. [CrossRef]
3. Zou, S.; Moldwin, M.B.; Coster, A.; Lyons, L.R.; Nicolls, M.J. GPS TEC observations of dynamics of the mid-latitude trough during substorms. *Geophys. Res. Lett.* **2011**, *38*, L14109. [CrossRef]
4. Polekh, N.; Zolotukhina, N.; Kurkin, V.; Zherebtsov, G.; Shi, J.; Wang, G.; Wang, Z. Dynamics of ionospheric disturbances during the 17–19 March 2015 geomagnetic storm over East Asia. *Adv. Space Res.* **2017**, *60*, 2464–2476. [CrossRef]
5. Brace, L.H.; Chappell, C.R.; Chandler, M.O.; Comfort, R.H.; Horwitz, J.L.; Hoegy, W.R. Fregion electron temperature signatures of the plasmapause based on Dynamics Explorer 1 and 2 measurements. *J. Geophys. Res. Space Phys.* **1988**, *93*, 1896–1908. [CrossRef]
6. Deminov, M.G.; Karpachev, A.T.; Annakuliev, S.K.; Afonin, V.V.; Smilauer, Y. Dynamics of the ionization troughs in the night-time subauroral F-region during geomagnetic storms. *Adv. Space Res.* **1996**, *17*, 141–145. [CrossRef]
7. Echer, E.; Korth, A.; Zong, Q.-G.; Fraünz, M.; Gonzalez, W.D.; Guarnieri, F.L.; Fu, S.Y.; Rème, H. Cluster observations of O+escape in the magnetotail due to shock compression effects during the initial phase of the magnetic storm on 17 August 2001. *J. Geophys. Res.* **2008**, *113*, A05209. [CrossRef]
8. Zeren, Z.; Cao, J.; Liu, W.; Fu, H.; Wang, T.; Zhang, X.; Shen, X. Storm time evolution of ELF/VLF waves observed by DEMETER satellite. *J. Geophys. Res. Space Phys.* **2014**, *119*, 2612–2622. [CrossRef]
9. Píša, D.; Parrot, M.; Santolik, O.; Menietti, J.D. EMIC waves observed by the low-altitude satellite DEMETER during the November 2004 magnetic storm. *J. Geophys. Res. Space Phys.* **2015**, *120*, 5455–5464. [CrossRef]
10. Yang, N.; Le, H.; Liu, L. Statistical analysis of the mid-latitude trough position during different categories of magnetic storms and different storm intensities. *Earth Planets Space* **2016**, *68*, 171. [CrossRef]

11. Bhattarai, N.; Chapagain, N.P.; Adhikari, B. Total Electron Content and Electron Density Profile Observations during Geomagnetic Storms using COSMIC Satellite Data. *Discovery* **2016**, *52*, 1979–1990.
12. Cherniak, I.; Zakharenkova, I.; Sokolovsky, S. Multi-Instrumental Observation of Storm-Induced Ionospheric Plasma Bubbles at Equatorial and Middle Latitudes. *J. Geophys. Res. Space Phys.* **2019**, *124*, 1491–1508. [CrossRef]
13. Wang, Q.; Huang, J.P.; Zhang, X.M.; Shen, X.H.; Yuan, S.G.; Zeng, L.; Cao, J.B. China Seismo-Electromagnetic Satellite search coil magnetometer data and initial results. *Earth Planet. Phys.* **2018**, *2*, 462–468. [CrossRef]
14. Aa, E.; Zhang, S.R.; Wang, W.; Erickson, P.J.; Qian, L.; Eastes, R.; Harding, B.J.; Immel, T.J.; Karan, D.K.; Daniell, R.E.; et al. Pronounced suppression and X-pattern merging of equatorial ionization anomalies after the 2022 Tonga volcano eruption. *J. Geophys. Res. Space Phys.* **2022**, *127*, e2022JA030527. [CrossRef] [PubMed]
15. Cai, X.; Burns, A.G.; Wang, W.; Qian, L.; Solomon, S.C.; Eastes, R.W.; McClintock, W.E.; Laskar, F.I. Investigation of a Neutral "Tongue" Observed by GOLD During the Geomagnetic Storm on May 11, 2019. *J. Geophys. Res. Space Phys.* **2021**, *126*, e2020JA028817. [CrossRef]
16. Balan, N.; Liu, J.Y.; Otsuka, Y.; Ram, S.T.; Luhr, H. Ionospheric and thermospheric storms at equatorial latitudes observed by CHAMP, ROCSAT, and DMSP. *J. Geophys. Res.* **2012**, *117*, A01313. [CrossRef]
17. Tulasi Ram, S.; Balan, N.; Veenadhari, B.; Gurubaran, S.; Ravindran, S.; Tsugawa, T.; Liu, H.; Niranjan, K.; Nagatsuma, T. First observational evidence for opposite zonal electric fields in equatorial E and F region altitudes during a geomagnetic storm period. *J. Geophys. Res.* **2012**, *117*, A09318. [CrossRef]
18. Kelley, M.C.; Vlasov, M.N.; Foster, J.C.; Coster, A.J. A quantitative explanation for the phenomenon known as storm-enhanced density. *Geophys. Res. Lett.* **2004**, *31*, L19809. [CrossRef]
19. Vlasov, M.; Kelley, M.C.; Kil, H. Analysis of ground-based and satellite observations of F-region behavior during the great magnetic storm of July 15, 2000. *J. Atmos. Sol.-Terr. Phys.* **2003**, *65*, 1223–1234. [CrossRef]
20. Blagoveshchensky, D.V.; Sergeeva, M.A. Ionospheric parameters in the European sector during the magnetic storm of August 25–26, 2018. *Adv. Space Res.* **2020**, *65*, 11–18. [CrossRef]
21. Mansilla, G.A.; Zossi, M.M. Ionospheric response to the 26 August 2018 geomagnetic storm along 280° E and 316° E in the South American sector. *Adv. Space Res.* **2022**, *69*, 48–58. [CrossRef]
22. Bolaji, O.S.; Fashae, J.B.; Adebiyi, S.J.; Owolabi, C.; Adebesin, B.O.; Kaka, R.O.; Ibanga, J.; Abass, M.; Akinola, O.O.; Adekoya, B.J.; et al. Storm time effects on latitudinal distribution of ionospheric TEC in the American and Asian-Australian sectors: August 25–26, 2018 geomagnetic storm. *J. Geophys. Res. Space Phys.* **2021**, *126*, e2020JA029068. [CrossRef]
23. Piersanti, M.; De Michelis, P.; Del Moro, D.; Tozzi, R.; Pezzopane, M.; Consolini, G.; Marcucci, M.F.; Laurenza, M.; Di Matteo, S.; Pignalberi, A.; et al. From the sun to the earth: August 25, 2018 geomagnetic storm effects. *Ann. Geophys.* **2020**, *38*, 703–724. [CrossRef]
24. Astafyeva, E.; Yasyukevich, Y.V.; Maletckii, B.; Oinats, A.; Vesnin, A.; Yasyukevich, A.S.; Syrovatskii, S.; Guendouz, N. Ionospheric disturbances and irregularities during the 25–26 August 2018 geomagnetic storm. *J. Geophys. Res. Space Phys.* **2022**, *127*, e2021JA029843. [CrossRef]
25. Cherniak, I.; Zakharenkova, I. Development of the Storm-Induced Ionospheric Irregularities at Equatorial and Middle Latitudes During the 25–26 August 2018 Geomagnetic Storm. *Space Weather* **2022**, *20*, e2021SW002891. [CrossRef]
26. Shen, X.; Zong, Q.; Zhang, X. Introduction to special section on the China Seismo-Electromagnetic Satellite and initial results. *Earth Planet. Phys.* **2018**, *2*, 439–443. [CrossRef]
27. Shen, X.H.; Zhang, X.; Yuan, S.G.; Wang, L.W.; Cao, J.B.; Huang, J.P.; Zhu, X.H.; Piergiorgio, P.; Dai, J.P. The state-of-the-art of the China Seismo-Electromagnetic Satellite mission. *Sci. China Technol. Sci.* **2018**, *61*, 634–642. [CrossRef]
28. Zhou, B.; Yang, Y.Y.; Zhang, Y.T.; Gou, X.C.; Cheng, B.J.; Wang, J.D.; Li, L. Magnetic field data processing methods of the China Seismo-Electromagnetic Satellite. *Earth Planet. Phys.* **2018**, *2*, 455–461. [CrossRef]
29. Cheng, B.J.; Zhou, B.; Magnes, W.; Lammegger, R.; Pollinger, A. High precision magnetometer for geomagnetic exploration onboard of the China Seismo-Electromagnetic Satellite. *Sci. China Technol. Sci.* **2018**, *61*, 659–668. [CrossRef]
30. Cao, J.B.; Zeng, L.; Zhan, F.; Wang, Z.G.; Wang, Y.; Chen, Y.; Meng, Q.C.; Ji, Z.Q.; Wang, P.F.; Liu, Z.W.; et al. The electromagnetic wave experiment for CSES mission: Search coil magnetometer. *Sci. China Technol. Sci.* **2018**, *61*, 653–658. [CrossRef]
31. Wang, H.; He, Y.F.; Lühr, H.; Kistler, L.M.; Saikin, A.A.; Lund, E.J.; Ma, S.-Y. Storm Time EMIC Waves Observed by Swarm and Van Allen Probe Satellites. *J. Geophys. Res. Space Phys.* **2019**, *124*, 293–312. [CrossRef]
32. Huang, J.P.; Lei, J.G.; Li, S.X.; Zeren, Z.M.; Li, C.; Zhu, X.H.; Yu, W.H. The Electric Field Detector (EFD) onboard the ZH-1 satellite and first observational results. *Earth Planet. Phys.* **2018**, *2*, 469–478. [CrossRef]
33. Yan, R.; Guan, Y.B.; Shen, X.H.; Huang, J.P.; Zhang, X.M.; Liu, C.; Liu, D.P. The Langmuir Probe Onboard CSES: Data inversion analysis method and first results. *Earth Planet. Phys.* **2018**, *2*, 479–488. [CrossRef]
34. Chu, W.; Huang, J.P.; Shen, X.H.; Wang, P.; Li, X.Q.; An, Z.H.; Xu, Y.B.; Liang, X.H. Preliminary results of the High Energetic Particle Package on-board the China Seismo-Electromagnetic Satellite. *Earth Planet. Phys.* **2018**, *2*, 489–498. [CrossRef]
35. Li, X.Q.; Xu, Y.B.; An, Z.H.; Liang, X.H.; Wang, P.; Zhao, X.Y.; Wang, H.Y.; Lu, H.; Ma, Y.Q.; Shen, X.H.; et al. The high-energy particle package onboard CSES. *Radiat. Detect. Technol. Methods* **2019**, *3*, 22. [CrossRef]
36. Ambrosi, G.; Bartocci, S.; Basara, L.; Battiston, R.; Burger, W.J.; Carfora, L.; Castellini, G.; Cipollone, P.; Conti, L.; Contin, A.; et al. The HEPD particle detector of the CSES satellite mission for investigating seismo-associated perturbations of the Van Allen belts. *Sci. China Technol. Sci.* **2018**, *61*, 643–652. [CrossRef]

37. Lin, J.; Shen, X.H.; Hu, L.C.; Wang, L.W.; Zhu, F.Y. CSES GNSS ionospheric inversion technique, validation and error analysis. *Sci. China Technol. Sci.* **2018**, *61*, 669–677. [CrossRef]
38. Cheng, Y.; Lin, J.; Shen, X.H.; Wan, X.; Li, X.X.; Wang, W.J. Analysis of GNSS radio occultation data from satellite ZH-01. *Earth Planet. Phys.* **2018**, *2*, 499–504. [CrossRef]
39. Chen, L.; Ou, M.; Yuan, Y.P.; Sun, F.; Yu, X.; Zhen, W.M. Preliminary observation results of the Coherent Beacon System onboard the China Seismo-Electromagnetic Satellite-1. *Earth Planet. Phys.* **2018**, *2*, 505–514. [CrossRef]
40. Zhang, X.; Qian, J.; Shen, X. Solar cycle variation of the electron density in the topside ionosphere at local nighttime observed by DEMETER during 2006–2008. *J. Geophys. Res. Space Phys.* **2014**, *119*, 3803–3814. [CrossRef]
41. Zhang, X. Electron Density Comparison Between IRI 2007 and DEMETER Satellite Data in Solar Minimum Year. *Terr. Atmos. Ocean. Sci.* **2014**, *25*, 559. [CrossRef]
42. Zhang, X.; Shen, X.; Liu, J.; Yao, L.; Yuan, G.; Huang, J. The asymmetrical features in electron density during extreme solar minimum. *Adv. Space Res.* **2014**, *54*, 2236–2248. [CrossRef]
43. Olsen, N.; Friis-Christensen, E.; Floberghagen, R.; Alken, P.; Beggan, C.; Chulliat, A.; Doornbos, E.; da Encarnacao, J.T.; Hamilton, B.; Hulot, G.; et al. The Swarm Satellite Constellation Application and Research Facility (SCARF) and Swarm data products. *Earth Planets Space* **2013**, *65*, 1189–1200. [CrossRef]
44. Schaer, S. Mapping and Predicting the Earth's Ionosphere Using the Global Positioning System. Ph.D. Thesis, Astronomical Institute University of Bern, Bern, Switzerland, 1999.
45. Ren, D.; Lei, J.; Zhou, S.; Li, W.; Huang, F.; Luan, X.; Dang, T.; Liu, Y. High-Speed Solar Wind Imprints on the Ionosphere During the Recovery Phase of the August 2018 Geomagnetic Storm. *Space Weather* **2020**, *18*, e2020SW002480. [CrossRef]
46. Akala, A.O.; Oyedokun, O.J.; Amaechi, P.O.; Simi, K.G.; Ogwala, A.; Arowolo, O.A. Solar Origins of August 26, 2018 Geomagnetic Storm: Responses of the Interplanetary Medium and Equatorial/Low-Latitude Ionosphere to the Storm. *Space Weather* **2021**, *19*, e2021SW002734. [CrossRef]
47. Chen, C.Y.; Liu, T.J.Y.; Lee, I.T.; Rothkaehl, H.; Przepiorka, D.; Chang, L.C.; Matyjasiak, B.; Ryu, K.; Oyama, K.-I. The Midlatitude Trough and the Plasmapause in the Nighttime Ionosphere Simultaneously Observed by DEMETER During 2006-2009. *J. Geophys. Res. Space Phys.* **2018**, *123*, 5917–5932. [CrossRef]
48. He, M.; Liu, L.; Wan, W.; Zhao, B. A study on the nighttime midlatitude ionospheric trough. *J. Geophys. Res.* **2011**, *116*, A05315. [CrossRef]
49. Deminov, M.G.; Karpachev, A.T.; Afonin, V.V.; Annakuliev, S.K. Dynamics of the midlatitude ionosphreic trough during storms: Main phase. *Geomag. Aeron.* **1995**, *35*, 69–77.
50. Deminov, M.; Shubin, V.N. Empirical Model of the Location of the Main Ionospheric Trough. *Geomagn. Aeron.* **2018**, *58*, 348–355. [CrossRef]